Original Article

Institution of MECHANICAL ENGINEERS

Journal of SYSTEMS AND CONTROL ENGINEERING

Proc IMechE Part I:
J Systems and Control Engineering
1–12

DOI: 10.1177/0959651817732502
journals.sagepub.com/home/pii
SAGE

Data-based double-feedforward controller design for a coupled parallel piezo nanopositioning stage

Zhao Feng, Jie Ling, Min Ming and Xiaohui Xiao

Abstract

Vibrations as well as cross-coupling effects severely hinder fast and accurate tracking for coupled parallel piezo nanopositioning stages. In this article, a data-based double-feedforward controller is proposed to reduce individual-axis repetitive errors and cross-coupling-caused errors simultaneously. The proposed approach utilizes modeling-free inversion-based iterative control to compensate repetitive errors and data-based feedforward decoupling controller to eliminate cross-coupling effect, which has the advantages of no need for accurate identified process and alleviating the difficulty in inversion of non-minimum phase systems. Comparative experiments were performed on a piezo parallel nanopositioning stage to validate the effectiveness of the proposed controller. Experimental results indicate that the cross-coupling errors are compensated significantly and the fast and accurate tracking can be achieved via implementing the proposed controller on planar raster scanning and XY star trajectory with different tracking periods.

Keywords

Parallel nanopositioning stage, cross-coupling effect, data-based control, feedforward control, trajectory tracking

Date received: 31 December 2016; accepted: 10 August 2017

Introduction

The piezo nanopositioning stage has been widely used in nanotechnology for the merits of its repeatable, reliable, and smooth motions.[1] The typical applications in industry are scanning probe microscopy (SPM),[2] atomic force microscope (AFM),[3] micromanipulation system,[4] and optical fiber alignment with the requirements of high-speed and high-accuracy tracking or positioning. The structure of piezo nanopositioning stages can be sorted into serial and parallel configurations.[5] Generally, for serial configuration, there exists cumulative errors and only one axis can achieve high-speed tracking for its high inertia.[6] However, high structural stiffness and bandwidth on all axes can be designed deliberately via parallel configuration. Therefore, the parallel nanopositioner has been widely used in commercial products.[6]

At low operating frequencies, the indigenous hysteresis nonlinearity limits the performance of nanopositioning stages.[7,8] Numerous methods have been proposed to compensate the adverse effect, such as charge control,[9] inverse model compensation,[10–12] solid mode,[8] and disturbance observer.[13] Besides, high-gain feedback controller is also an effective method to suppress hysteresis which has been validated in many literatures.[7,14,15] However, for fast and accurate tracking of the coupled parallel piezo nanopositioning stages, the vibration in individual axis and cross-coupling effect between axes become the main obstacles. As the motion speed increases, the vibrations become violent especially when operating frequency approaches to the first resonant mode of the nanopositioner, which damages the motion accuracy seriously. Furthermore, the performance is also deteriorated dramatically by cross-coupling effect, which has been elaborated by the experimental data.[16] In order to reduce cross-coupling errors, different decoupling structures have been studied.[17–19] However, only at low operating frequencies, the cross-coupling error is migrated

Hubei Key Laboratory of Waterjet Theory and New Technology, Wuhan University, Wuhan, P.R. China

Corresponding author:
Xiaohui Xiao, Hubei Key Laboratory of Waterjet Theory and New Technology, Wuhan University, Wuhan 430072, Hubei Province, P.R. China.
Email: xhxiao@whu.edu.cn

significantly and it still cannot be ignored as motion speed increases.

In order to suppress the lightly damped vibrational modes, several fix-structure feedback damping controllers have been designed for its simplification and practicability for application. These include positive position feedback,[20] resonant control,[21] integral resonant control,[22] and delayed position feedback control.[14] Besides, general model-based control laws can also be used, such as loop-shaping approach[23] and input shaper,[24] which have been designed with accurate modeling of the system. For the most part, the cross-coupling effect is always neglected for multiple-input multiple-output (MIMO) systems.[20,22] Recently, feedback controllers taking cross-coupling effect into consideration have been proposed to handle the vibration-caused errors and minimize interactive effect simultaneously.[25,26] These controllers still depend on the accurate modeling, and the feedback controllers alone may not achieve the anticipated performance in practice.

Besides, it should be noted that the integration with feedforward controller can improve the tracking performance compared with the use of feedback alone because of some practical and fundamental algebraic restrictions.[27] For most applications, the nanopositioning stage executes the same motion repetitively. Therefore, it is natural to use iterative learning control (ILC) to learn from previous iterations and modify the control force to improve tracking performance.[28,29] Bristow et al.[30] proposed a time-varying Q-filter ILC for high-bandwidth tracking. The frequency-domain formulated inversion-based ILC was implemented to compensate the individual-axis vibration and cross-coupling effect.[31] The above control strategies depend on the accuracy of dynamic modeling because of the need for plant inversion. However, with the existence of non-minimum phase (NMP) zeros and model uncertainty, plant inversion may be difficult to be implemented. Although the proportional (P-), derivative (D-), and proportional–derivative (PD)-type ILC can also be implemented without accurate model, the convergence speed is lower than model-inversion ILC.[29] To tackle this problem, Kim and Zou[32] proposed the modeling-free inversion-based iterative control (MIIC) approach for high-speed output tracking. However, MIIC can only be applied to single-input single-output (SISO) systems or MIMO systems without coupling. For fast and accurate tracking, the cross-coupling errors from other axes can affect the inverse model updated according to the measured input–output data with the increase in motion speed and cannot be compensated through iterations. Bolder et al.[33] and Heertjes et al.[34] proposed a data-driven multivariable ILC and gradient approximation–based feedforward controller, respectively, but these methods need tedious experiments to calculate gradient. A feedforward decoupling controller (FDC) has been also proposed to reduce the cross-coupling errors in condition of accurate system model of the hard disk drives.[35] However, it should be noted that this decoupling controller is unstable when the system has NMP zeros.

To this end, the data-based double-feedforward controller is proposed in this article for fast and accurate tracking of a coupled parallel piezo nanopositioning stage, where the data-based feedforward decoupling controller (DFDC) is utilized to eliminate the cross-coupling errors, and trajectory tracking is realized by implementing MIIC to remove repetitive errors and disturbances in each axis. Comparing with the feedback-alone control scheme, the proposed controller can track repetitive trajectory effectively at higher operating frequencies for coupled MIMO systems. Furthermore, the controller is designed through collecting data from experiments, no matter the plant is NMP or not, which alleviates the dependence for accurate modeling, model-based plant inversion and tedious calculation in comparison with the methods in Bolder et al.,[33] Heertjes et al.[34] and Zheng et al.[35]

The rest of this article is continued as follows. The individual vibration and cross-coupling effect problems are presented in "Problem formulation." The method to design the controller is described in "Controller design." Experiments and comparisons of the results are elaborated in "Application to a piezo nanopositioner" and the "Conclusion" concludes the article.

Problem formulation

Dynamic model

For piezo nanopositioning stages, the cascade connection of hysteresis nonlinearity and linear vibration dynamics is a common approach to represent the complex model.[11,36] However, it needs to construct hysteresis model and calculate its inversion, which is complex to implement in practice. In this article, the complex dynamic is developed by regarding the hysteresis as an external disturbance added to a linear vibration dynamic to avoid hysteresis modeling.[13,37] Therefore, in order to simplify the presentation, the transfer function of the coupled parallel nanopositioner without hysteresis nonlinearity is described as a linear 2×2 diagonal domain plant $P(j\omega)$ in this article, which can be expressed as

$$P(j\omega) = \begin{bmatrix} P_{xx}(j\omega) & P_{xy}(j\omega) \\ P_{yx}(j\omega) & P_{yy}(j\omega) \end{bmatrix} \tag{1}$$

Therefore, the open-loop output displacement without hysteresis nonlinearity $d_x(t)$ and $d_y(t)$ can be described as

$$out_x(\omega) = P_{xx}(j\omega)u_x(\omega) + P_{xy}(j\omega)u_y(\omega) \tag{2}$$

$$out_y(\omega) = P_{yy}(j\omega)u_y(\omega) + P_{yx}(j\omega)u_x(\omega) \tag{3}$$

where $out_x(\omega)$, $u_x(\omega)$, $out_y(\omega)$, and $u_y(\omega)$ denote the Fourier transforms of $out_x(t)$, $u_x(t)$, $out_y(t)$, and $u_y(t)$, respectively. $P_{xx}(j\omega)$ and $P_{yy}(j\omega)$ are the dominant dynamics and $P_{yx}(j\omega)$ and $P_{xy}(j\omega)$ present the coupled

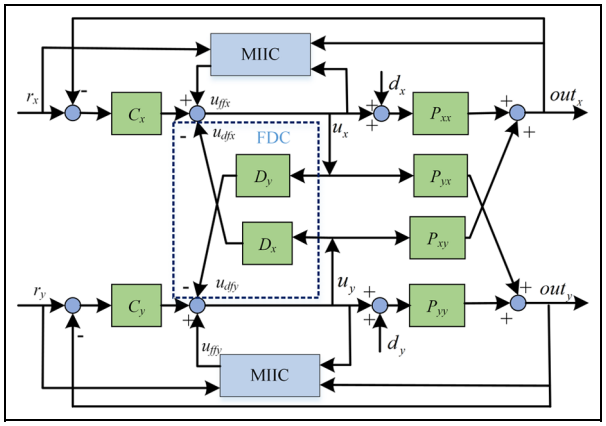

Figure 1. Block diagram of the control scheme.

terms as is demonstrated in Figure 1. As is seen from equations (2) and (3), the $out_x(\omega)$ and $out_y(\omega)$ are determined by both the diagonal dominant dynamics and non-diagonal dominant dynamics, that is, coupled terms.

Control scheme

To reduce cross-coupling errors in a MIMO system, several decoupling feedback controllers have been proposed.[38,39] However, due to the complexity in practical applications and internal uncertainty in feedback loop, these control schemes are difficult to design for high performance. Therefore, to avoid feedback loop redundancy and simplify the controller design, the MIMO system should be decoupled as several SISO systems via decoupling feedforward control. As is shown in Figure 1, the baseline feedback controllers $C_x(j\omega)$ and $C_y(j\omega)$ guarantee robust stability and suppress unknown disturbance for each axis, and the model-based FDC $D_x(j\omega)$ and $D_y(j\omega)$ attenuates the cross-coupling errors to decouple the plant. Besides, the feedforward controllers used to compensate for individual error are also essential to improve the tracking performance further. $u_{ffx}(\omega)$, $u_{dfx}(\omega)$, $u_{ffy}(\omega)$, $u_{dfy}(\omega)$, $u_{fbx}(\omega)$, and $u_{fby}(\omega)$ are the Fourier transforms of $u_{ffx}(t)$, $u_{dfx}(t)$, $u_{ffy}(t)$, $u_{dfy}(t)$, $u_{fbx}(t)$, and $u_{fby}(t)$, respectively. The x axis control input $u_x(\omega)$ is the sum of feedback input $u_{fbx}(\omega)$, the feedforward input $u_{ffx}(\omega)$, and the decoupling feedforward control input $u_{dfx}(\omega)$

$$u_x(\omega) = u_{fbx}(\omega) + u_{ffx}(\omega) + u_{dfx}(\omega) \tag{4}$$

According to Figure 1, the output of x axis without $d_x(t)$ in the closed-loop system can be obtained as

$$\begin{aligned} out_x(\omega) &= T_x(j\omega)r_x(\omega) + S_x(j\omega)P_{xx}(j\omega)u_{ffx}(\omega) \\ &+ S_x(j\omega)P_{xy}(j\omega)u_y(\omega) - S_x(j\omega)P_{xx}(j\omega)u_{dfx}(\omega) \end{aligned} \tag{5}$$

where S_x and T_x are the sensitivity function and complementary sensitivity function, respectively

$$T_x(j\omega) = \frac{P_{xx}(j\omega)C_x(j\omega)}{1 + P_{xx}(j\omega)C_x(j\omega)} \tag{6}$$

$$S_x(j\omega) = \frac{1}{1 + P_{xx}(j\omega)C_x(j\omega)} \tag{7}$$

Hence, the error of x axis is expressed as

$$\begin{aligned} e_x(\omega) &= S_x(j\omega)r_x(\omega) - S_x(j\omega)P_{xx}(j\omega)u_{ffx}(\omega) \\ &- S_x(j\omega)P_{xy}(j\omega)u_y(\omega) + S_x(j\omega)P_{xx}(j\omega)u_{dfx}(\omega) \end{aligned} \tag{8}$$

In order to eliminate cross-coupling effect, equation (9) should be satisfied, that is

$$-S_x(j\omega)P_{xy}(j\omega)u_y(\omega) + S_x(j\omega)P_{xx}(j\omega)u_{dfx}(\omega) = 0 \tag{9}$$

In terms of this, the model-based FDC for x axis is deduced as

$$D_x(j\omega) = \frac{P_{xy}(j\omega)}{P_{xx}(j\omega)} \tag{10}$$

Similarly, the model-based FDC for y axis is described as

$$D_y(j\omega) = \frac{P_{yx}(j\omega)}{P_{yy}(j\omega)} \tag{11}$$

The decoupled system with two SISO plants can be obtained via $D_x(j\omega)$ and $D_y(j\omega)$. Besides, u_{ffx} and u_{ffy} are also implemented to improve the tracking performance for each axis. For repetitive trajectory commonly used in nanopositioner, the hysteresis nonlinearity $d_x(t)$ and $d_y(t)$ can also be treated as repetitive disturbance,[16] which will be migrated by u_{ffx} and u_{ffy}. However, it should be noted that if P_{xx} or P_{yy} has NMP zeros, model-based FDC $D_x(j\omega)$ or $D_y(j\omega)$ is unstable, which will result in divergence of the system.

Contribution of this article

In brief, the contribution of this article is three-fold in view of the requirements for a coupled parallel piezo nanopositioning stage.

1. DFDC is proposed to design the FDC although NMP zeros exist via collecting data through experiments.
2. The design procedure of the proposed data-based double-feedforward controller is constructed to reduce individual-axis repetitive errors and cross-coupling-caused errors simultaneously for fast and accurate trajectory tracking.
3. The proposed controller is validated on a parallel nanopositioning stage via comparative experiments.

Controller design

Modeling-free inversion iterative control

The MIIC algorithm is a modeling-free ILC method through inversing the plant in frequency domain via

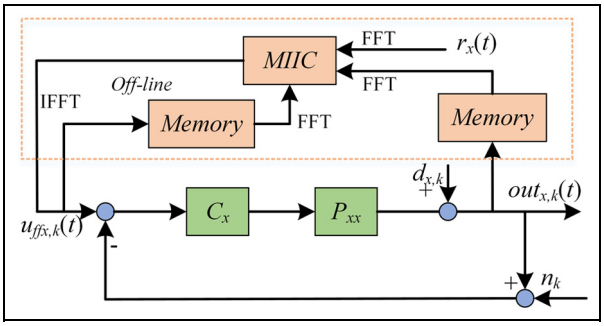

Figure 2. Block diagram of the implementation for MIIC.

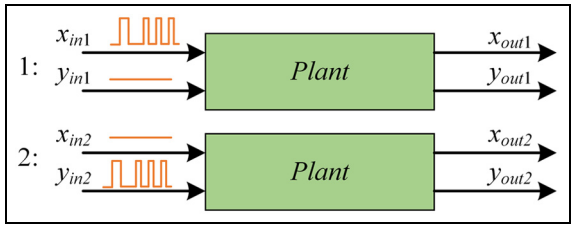

Figure 3. The block diagram for ETFE.

collected data in each ILC iteration.[32] The control law can be expressed as

$$u_{ffx,0}(j\omega) = \alpha r_x(j\omega), \quad k = 0$$
$$u_{ffx,k}(j\omega) = \begin{cases} \dfrac{u_{ffx,k-1}(j\omega)}{out_{ffx,k-1}(j\omega)} r_x(j\omega) \\ \text{when} \quad out_{ffx,k-1}(j\omega) \neq 0 \\ \text{and } r_x(j\omega) \neq 0, k \geqslant 1 \\ 0 \quad \text{otherwise} \end{cases} \tag{12}$$

where $\alpha \neq 0$ is a prechosen constant that is usually the reciprocal of the estimated DC gain of the system. In this article, α is chosen as 1. Generally, for the first iteration, the input signal is the anticipated trajectory $r_x(t)$ and $uff_{x,k}(t)$ is injected to the system subsequently via calculating equation (12). For traditional ILC, the dynamics model and the modeling process are needed to achieve rapid convergence. However, MIIC removes modeling of the plant through iterative update by making use of the collected input–output data in the iterative process. The convergence of MIIC depends on the additional disturbance and measurement noise, that is, noise/disturbance-to-signal ratio (NSR), given by[32]

$$\left| \frac{out_{x,k-1}(j\omega)}{r_x(j\omega)} \right| < 1 - \frac{\sqrt{2}}{2} \tag{13}$$

The implementation of MIIC is presented in Figure 2. The measured time domain signals are transformed into frequency domain via fast Fourier transform (FFT), and the updated control input in time domain is obtained via inverse fast Fourier transform (IFFT), repeating the cycle. It should be noted that when using FFT, the time domain signal is truncated by a rectangular window. If the input is a periodic signal, the non-integral period truncation may result in spreading of energy from one frequency into adjacent ones, which will affect the iterative process, even lead to divergence. Therefore, proper signal-processing techniques have to be considered to avoid the pitfall in FFT. In this article, the Hanning window is utilized to truncate signal to alleviate energy leakage. It should be noted that in order to avoid errors caused by vibrations that deteriorate FFT, the control algorithm is implemented on the damped plant, that is, the closed-loop system in this article.

Data-based FDC

Generally, the transfer functions of model-based feedforward controllers, such as equations (10) and (11), can be calculated by accurate system identification with infinite impulse response (IIR) structure. However, if there exist NMP zeros, the decoupling controllers are unstable. Therefore, in this article, the finite impulse response (FIR) structure is chosen to model the decoupling feedforward controllers, which remain stable with poles in the origin and can approximate $D_x(j\omega)$ and $D_y(j\omega)$ via various zeros. An FIR tuning method using gradient-based approach was developed to reduce cross-coupling errors.[34] However, the method needs extra iteration to run the plant and is difficult to combine with ILC. In this article, a simpler method is proposed and the design of DFDC is based on empirical transfer-function estimate (ETFE).[40]

To obtain the data from plant, the pseudo-random binary signal (PRBS) with white spectrum is the input signal via the two-run method as described in Figure 3. For the first experiment, PRBS is injected into the x axis and zero input for the y axis. The signal input to the plant is reversed for the second experiment. Through the collected data, in the frequency samples $k \in [0, M-1]$, the ETFE plants from x to x and y to x are denoted as $\hat{P}_{xx}(k)$ and $\hat{P}_{yx}(k)$

$$\hat{P}_{xx}(k) = \frac{x_{out1}(k)}{x_{in1}(k)} \tag{14}$$

$$\hat{P}_{yx}(k) = \frac{x_{out2}(k)}{y_{in2}(k)} \tag{15}$$

where $x_{out1}(k)$, $y_{in2}(k)$, $x_{out2}(k)$, and $y_{in2}(k)$ are the discrete Fourier transforms (DFT). Therefore, according to equation (10), the ETFT of decoupling controller for x axis is described in equation (16)

$$\hat{D}_x(k) = \frac{x_{out2}(k)}{x_{out1}(k)} \tag{16}$$

where

$$x_{out1}(k) = \sum_{n=0}^{M-1} x_{out1}(n) e^{-j2\pi kn/M} \tag{17}$$

$$x_{out2}(k) = \sum_{n=0}^{M-1} x_{out2}(n)e^{-j2\pi kn/M} \tag{18}$$

for $k = 0, 1, \ldots, M-1$. To obtain the controller with FIR structure, the inverse discrete Fourier transform (IDFT) is calculated via unit impulse response $d_{xi}(n)$

$$d_{xi}(n) = \frac{1}{M}\sum_{k=0}^{M-1} \hat{D}_x(k)e^{j2\pi kn/M} \tag{19}$$

where $n = 0, 1, \ldots, M-1$. Then, decoupling controller can be expressed in the z domain as

$$D_{xifir}(z^{-1}) = \sum_{k=0}^{M-1} d_{xi}(n)z^{-n} \tag{20}$$

Because the collected data are truncated by the rectangular window that can cause side-lobes in frequency domain, the Hanning window is adopted for accurate estimation in this article. Then, a windowed controller $d_{xwi}(n)$ can be described as

$$d_{xwi}(n) = w(n)d_{xi}(n) \tag{21}$$

and $w(n)$ is the window function with length M determined by trial and error. The representation of the window function $W(k)$ is found in frequency domain as

$$W(k) = \left[\sum_{n=0}^{M-1} w(n)e^{-j2\pi kn/M}\right] e^{-j(2\pi kn/M)(M/2)} \tag{22}$$

Due to the shift of the window function, $D_{xifir}(z^{-1})$ should be shifted before windowing, which means that $D_{xifir}(z^{-1})$ is delayed by $M/2$ step. Then, the DFDC of x axis $D_{xifir}(z^{-1})$ can be obtained by

$$D_{xfir}(z^{-1}) = W(z^{-1}) * \left[z^{-M/2}D_{xifir}(z^{-1})\right] \tag{23}$$

where $*$ indicates convolution. We can also use the same method to obtain $D_{yfir}(z^{-1})$. Hereto, the overall design procedure is described as follows:

1. Collect two sets of the experimental data as is described in Figure 3, design DFDC for x axis and y axis, respectively, and implement it via replacing D_x and D_y by $D_{xfir}(z^{-1})$ and $D_{yfir}(z^{-1})$, respectively.
2. Design the baseline feedback controllers for the dominant dynamics of the plant.
3. Implement MIIC to the closed-loop system with DFDC and start iteration until the required performance.

For the design of double-feedforward controller, MIIC and DFDC, the experiment data are made use of without accurate modeling, that is, data-based feedforward control and the FIR structure used in DFDC avoid the effect of NMP zeros.

Application to a piezo nanopositioner

Experimental setup

The nanopositioning stage (P-561.3CD, Physik Instrumente), used in the experiment, is a piezoelectric stack-actuated platform based on parallel-kinematic design with 100 μm stroke of each axis. The control input voltage (0–10 V) is produced by 16-bit digital-to-analog converters (DACs) of the data acquisition card (PCI 6289; National Instrument) and subsequently amplified via a piezo amplifier module (E-503.00; Physik Instrumente) with a fixed gain of 10 to provide excitation voltage (0–100 V). The displacement of the output 0–10 V is read via a sensor monitor (E-509.C3A; Physik Instrumente) and is passed to the data acquisition card (PCI 6289; National Instruments) equipped with 18-bit analog-to-digital converters (ADCs). The control algorithm was designed in MATLAB/Simulink block diagram on develop PC and then downloaded and executed in real time on the target PC (CPU: Intel Core i5 at 3.3 GHz). In this work, the sampling frequency is set to 10 kHz. Figure 4 shows the experimental setup.

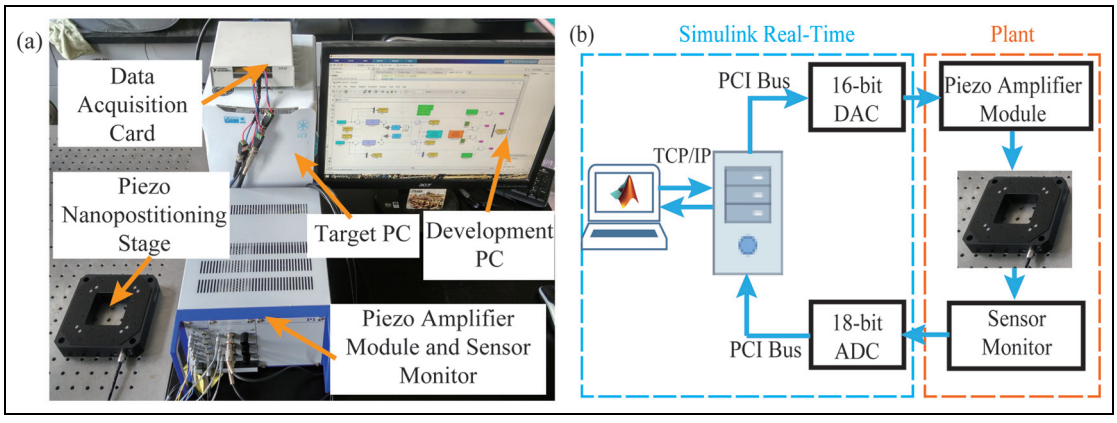

Figure 4. The experimental setup of the parallel nanopositioning stage: (a) experimental platform and (b) block diagram.

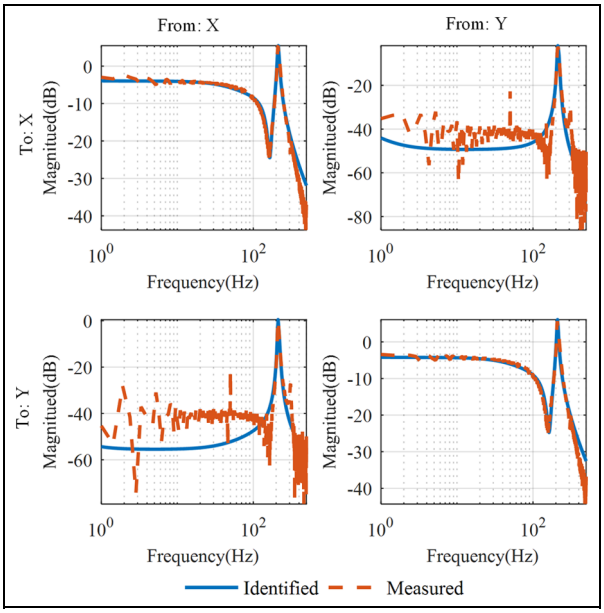

Figure 5. The measured and the identified model amplitude frequency responses.

The linear vibration model of the nanopositioning stage is obtained by applying a 100 mV swept sine wave between 0.1 and 500 Hz to both x and y axes. Here, the low amplitude of the input is intended to minimize the hysteresis nonlinearity. Then, the system identification toolbox of MATLAB is used to identify the dynamic model. The transfer functions of $P_{xx}(s)$ and $P_{yy}(s)$ are obtained as follows with $s = j\omega$

$$P_{xx}(s) = P_{yy}(s) = k \cdot \frac{\prod_{i=1}^{6}(s - z_i)}{\prod_{j=1}^{8}(s - p_j)}, \quad \text{with } k = -18,684$$
$$z_i = \{7345.7, -3744.3, -47.22 \pm 978.14, -15.02, -1.16\}$$
$$p_j = \{-34.03 \pm 1327.6, -337.79 \pm 879.67, -614.65 \pm 110.73, -14.68, -1.1384\} \quad (24)$$

Figure 5 shows the match between the measured open-loop frequency response and the frequency responses of identified models. It demonstrates that at frequency 211 Hz, both oscillation and cross-coupling-caused errors are large which will deteriorate the performance severely. Besides, the plant is an NMP system, as is shown in equation (24), which may be a problem for model-based feedforward controller design.

Controller implementation

In order to obtain $D_{xifir}(z^{-1})$ and $D_{yifir}(z^{-1})$ to decouple the parallel system, the two-run method in Figure 3 and the Hanning window with length $M = 60$ was adopted to design DFDC. The bode diagram of identified decoupler and DFDC is demonstrated in Figure 6, which indicates that the proposed method can capture the dynamics of the decouplers well, especially at higher frequencies where cross-coupling effect is large.

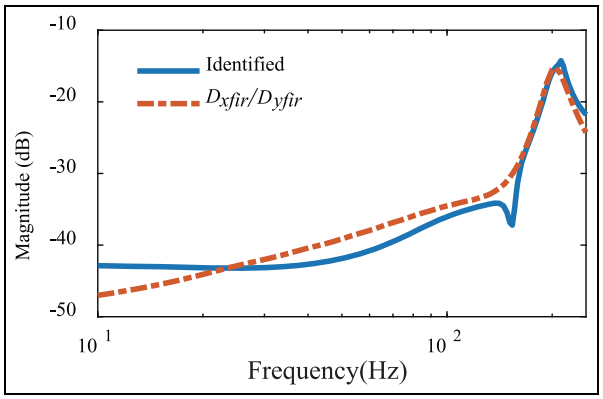

Figure 6. Comparison of identified decoupler and proposed DFDC.

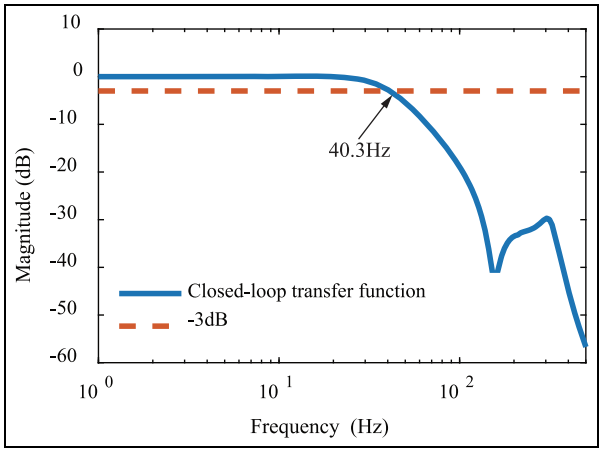

Figure 7. Bode diagram of closed-loop transfer function of the decoupled system.

Besides, to suppress hysteresis nonlinearity and unknown disturbance, a high-gain feedback controller was designed in this article. The notch filter can improve the stability margin, and then, a high-gain integral controller was developed to suppress the hysteresis and improve tracking performance. The transfer function of feedback controller is given as

$$C_x(s) = C_y(s) = \frac{400s^2 + 2.655e4s + 7.05e8}{s^3 + 400s^2 + 4e6s} \quad (25)$$

and discretized via zero-order holder (ZOH) method for practical implementation. The bode diagram of closed-loop transfer function of the decoupled system is displayed in Figure 7, from which the closed-loop bandwidth is 40.3 Hz. For high-speed tracking, feedback controller alone may not meet the required performance because of the limitation of bandwidth and phase lag. Therefore, MIIC is also adopted according to the design procedure.

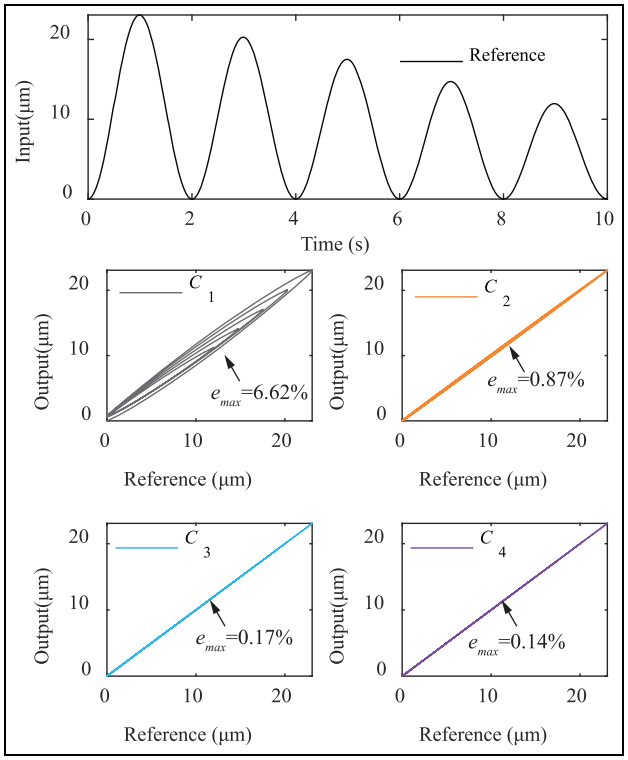

Figure 8. Experimental results of hysteresis curves.

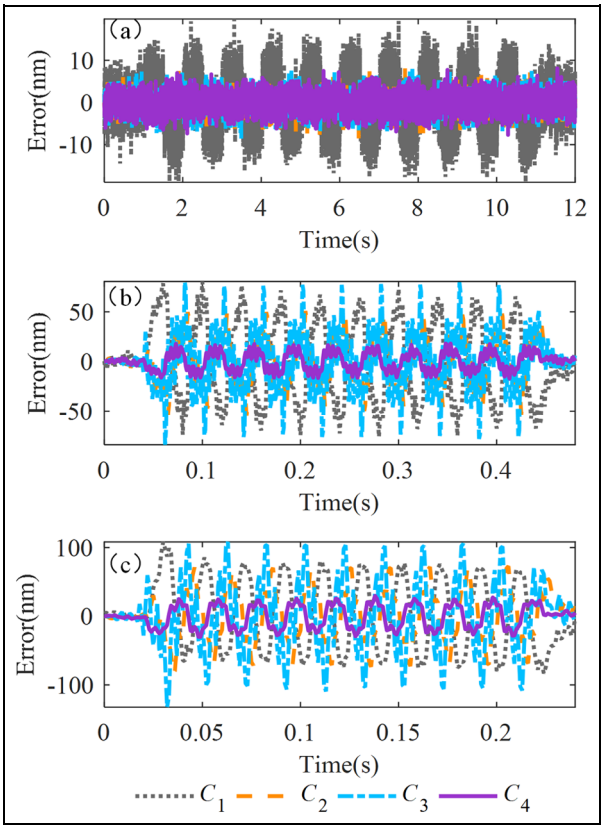

Figure 9. Cross-coupling errors of *x* axis with different frequencies are input into *y* axis: (a) 1 Hz triangle, (b) 25 Hz triangle, and (c) 50 Hz triangle.

Experimental results

To evaluate the experimental performance, the root-mean-square (RMS) error and maximum (MAX) error are adopted in this article. Furthermore, four experimental conditions with different controllers listed below also have been developed for comparisons.

1. C_1: experimental results without controller, that is, open-loop test.
2. C_2: experimental results with baseline feedback controllers C_x and C_y.
3. C_3: experimental results with baseline feedback controllers and MIIC.
4. C_4: the proposed data-based double-feedforward controller.

Suppression of hysteresis nonlinearity. Experimental results of hysteresis curves with 0.5 Hz varying amplitude sinusoidal signal for x axis are demonstrated in Figure 8. Without compensation C_1, the effect of hysteresis is significant with the relative maximum error 6.62%. The relative maximum error with C_2 is 0.87%, which indicates that the high-gain feedback controller can suppress quasi-static hysteresis effectively. For C_3 and C_4, the relative maximum errors reduce to 0.17% and 0.14%, respectively, because that the hysteresis can be treated as repetitive disturbance for MIIC and is migrated through iteration.[27] As a sequence, the effect of hysteresis is neglected for C_2, C_3, and C_4 in the following section.

Table 1. Cross-coupling errors of *x* axis.

Statistical errors (nm)		1 Hz	25 Hz	50 Hz
C_1	RMS	6.156	39.479	50.024
	MAX	19.7762	80.539	108.179
C_2	RMS	2.204	22.545	37.725
	MAX	8.067	50.812	72.789
C_3	RMS	2.238	30.895	51.952
	MAX	7.973	80.101	108.129
C_4	RMS	2.052	8.915	16.741
	MAX	8.089	18.452	29.685

RMS: root mean square.

Compensation of cross-coupling errors. To evaluate the effect of DFDC to compensate cross-coupling errors, Figure 9 shows the experimental results when 1, 25, and 50 Hz triangle waves with the peak-to-peak amplitude of 20 μm were injected into y axis. Table 1 shows the RMS errors and MAX errors. It is obvious that the cross-coupling errors increase as the input frequencies increase with C_1, which validates that the cross-coupling effect becomes prominent at higher operating frequencies. At low frequency of 1 Hz, the RMS errors are less than 10 nm and the MAX errors are less than 20 nm with four conditions for the low interactive effect. However, the error with C_3 exceeds the condition with C_2 and C_4 above 25 Hz because that the cross-coupling-caused errors mixed with the x axis

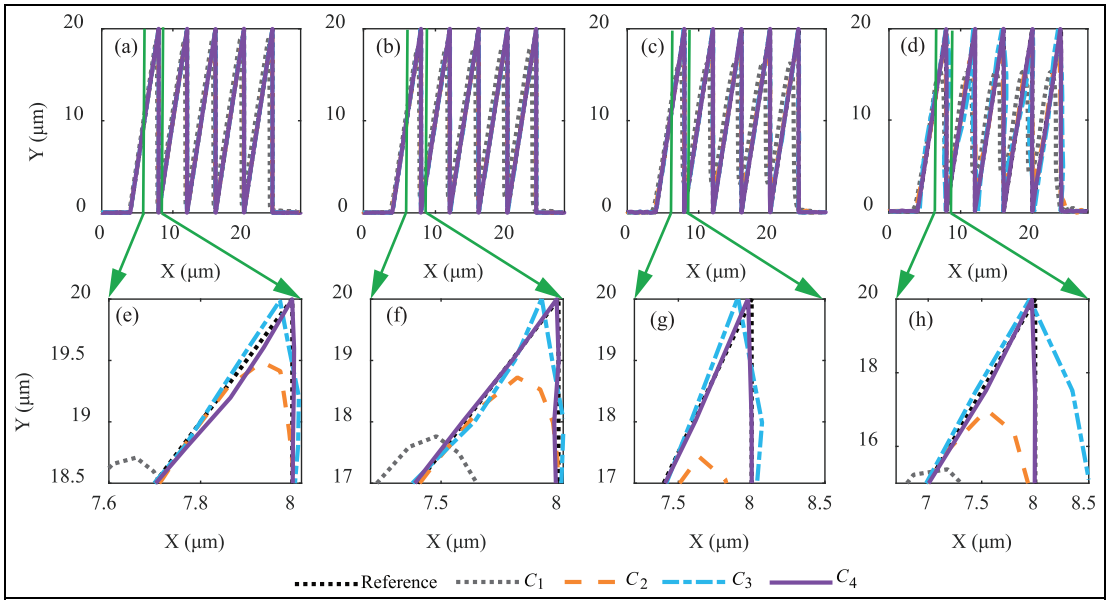

Figure 10. Raster scanning tracking results: (a) 0.7 s tracking period, (b) 0.28 s tracking period, (c) 0.14 s tracking period, (d) 0.112 s tracking period, and (e)–(h) the zoom-in view.

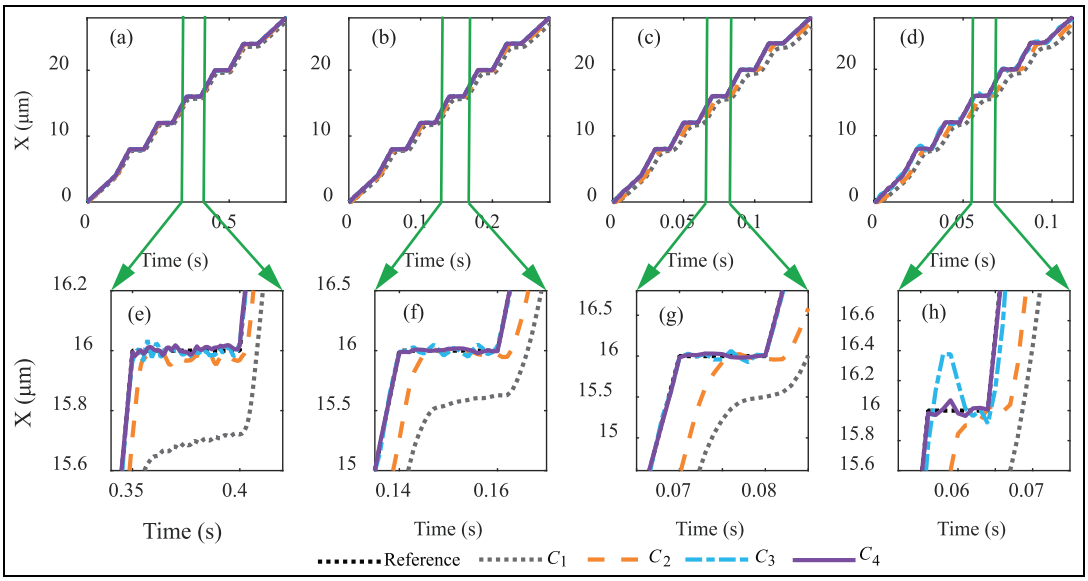

Figure 11. Raster scanning tracking results of *x* axis: (a) 0.7 s tracking period, (b) 0.28 s tracking period, (c) 0.14 s tracking period, (d) 0.112 s tracking period, and (e–h) the zoom-in view.

affect the iterative update using the measured input–output data of MIIC without DFDC, which indicates that C_3 has no ability to eliminate cross-coupling-caused errors. The errors with C_4 are all below 18 nm for RMS errors and 30 nm for MAX errors from 1 to 50 Hz, which declares that the proposed controller can compensate cross-coupling errors significantly.

Fast and accurate tracking results.

Raster scanning. The raster scanning results with different controllers are plotted in Figure 10, and the individual-axis tracking results are demonstrated in Figures 11 and 12, respectively. It is clear that the controller with C_4 achieves the best performance for 0.7, 0.28, 0.14, and 0.112 s tracking period, respectively. The RMS errors and MAX errors for x and y axes were recorded in Table 2. The performance with C_1 is the worst for the lightly damped resonant mode and hysteresis nonlinearity. For C_2, the errors at the corner are large for the rolling-off and phase lag at high frequency. The RMS errors and MAX errors of x and y axes are equal to 3.79% and 29.06% of the total scan range of 27.75 μm and 6.84% and 46.34% of the total scan range of 20 μm for y axis, which are unacceptable for fast and accurate tracking at 0.112 tracking period.

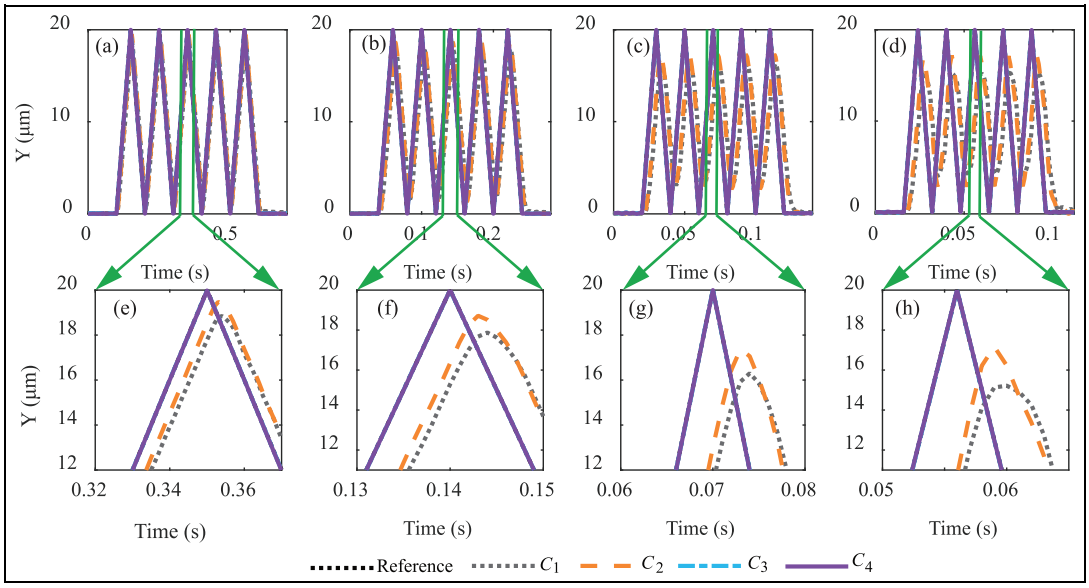

Figure 12. Raster scanning tracking results of *y* axis: (a) 0.7 s tracking period, (b) 0.28 s tracking period, (c) 0.14 s tracking period, (d) 0.112 s tracking period, and (e)–(h) the zoom-in view.

Table 2. Raster scanning tracking results.

		x axis				*y* axis			
Statistical errors (nm)		0.7 s	0.28 s	0.14 s	0.112 s	0.7 s	0.28 s	0.14 s	0.112 s
C_1	RMS	498.28	886.00	1409.50	1649.95	1424.1	3209.41	5496.82	6409.44
	MAX	820.65	1499.30	2416.61	2886.92	2357.12	4859.92	8853.21	11140.10
C_2	RMS	197.83	486.34	893.44	1095.40	1182.91	2789.01	4927.02	5812.52
	MAX	327.68	760.16	1517.12	1899.12	1493.12	3712.32	7270.04	9269.71
C_3	RMS	13.69	30.74	52.79	229.66	12.02	11.7034	25.28	23.40
	MAX	49.53	107.60	158.32	428.01	38.08	36.28	49.58	55.24
C_4	RMS	11.23	17.46	25.32	29.35	11.94	10.33	21.31	23.14
	MAX	35.55	100.49	209.55	243.65	37.64	24.08	49.40	56.16

RMS: root mean square.

The implement of MIIC could reduce errors at low operating frequencies. At 0.7, 0.28, and 0.14 s tracking period, the RMS error and MAX errors are below 53 and 159 nm for both x axis and y axis with C_3. However, as the tracking frequency increases, the performance of MIIC is deteriorated for the fact that the cross-coupling effect is obvious at high frequency although MIIC has compensated the individual vibrations and hysteresis nonlinearity.

The proposed controller C_4 achieves the RMS error with 29.35 nm and MAX error with 243.65 nm for x axis at 0.112 s tracking period. Comparing with the RMS error with 229.66 nm and MAX error with 428.01 nm for C_3, it is clear that DFDC weakens the effect of cross-coupling significantly. Similar results are for y axis. It is noted that RMS errors and MAX errors are at low frequencies, that is, 0.14 s and 0.112 tracking period; the errors of x axis are larger than y axis because that the input of y axis is a triangle signal that contains higher frequency components which contribute to cross-coupling errors on x axis.

XY star trajectory tracking results. To evaluate the ability of the proposed controller to track complex planar trajectory, a XY star trajectory was used for experiment. Figure 13 depicts the tracking results in XY plane using different controllers with different tracking periods. The individual-axis tracking results are demonstrated in Figures 14 and 15, respectively. Tracking errors with C_2 are large below 0.1 s tracking period because of phase lag and bandwidth limitation. For tracking period at 1 and 0.1 s, the tracking errors obtained using C_3 are close to the errors using the proposed controller (see Table 3). However, at high tracking rates with 0.04 and 0.03 s, the performance with C_3 becomes worse with RMS errors above 72 nm and MAX errors above 168 nm for both x and y axes.

As is mentioned before, cross-coupling effect between axes would be large at high frequencies, which can influence the removal of modeling errors for individual axis. The cross-coupling errors cannot be compensated by MIIC. The tracking results in Table 3 show that using the proposed controller C_4, accurate tracking can be achieved, even at high tracking rates. The RMS

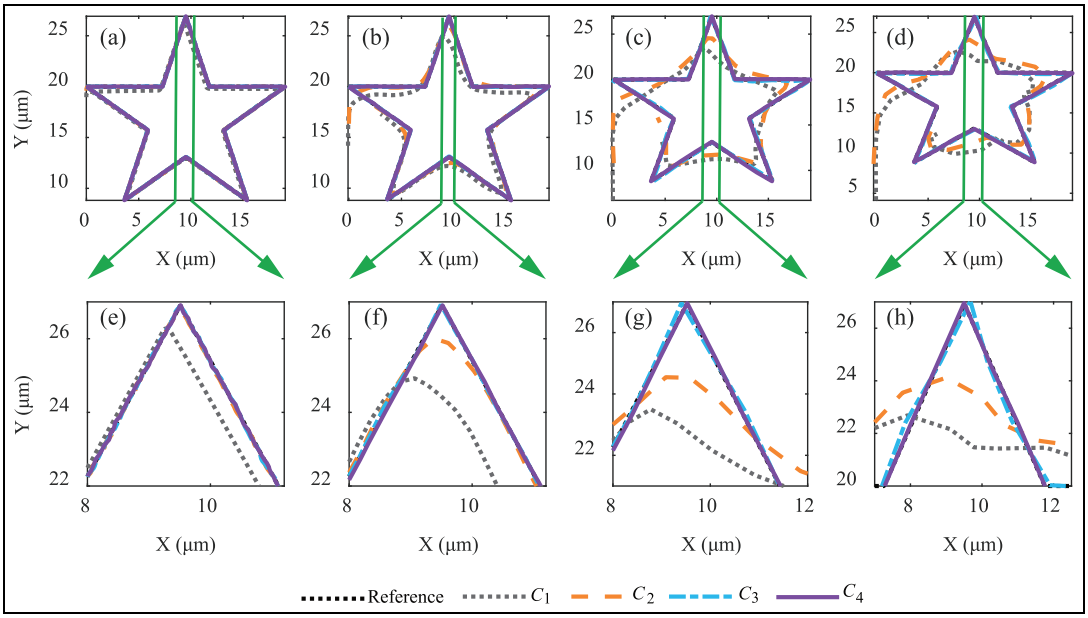

Figure 13. Star trajectory tracking results: (a) 1 s tracking period, (b) 0.1 s tracking period, (c) 0.04 s tracking period, (d) 0.03 s tracking period, and (e)–(h) the zoom-in view.

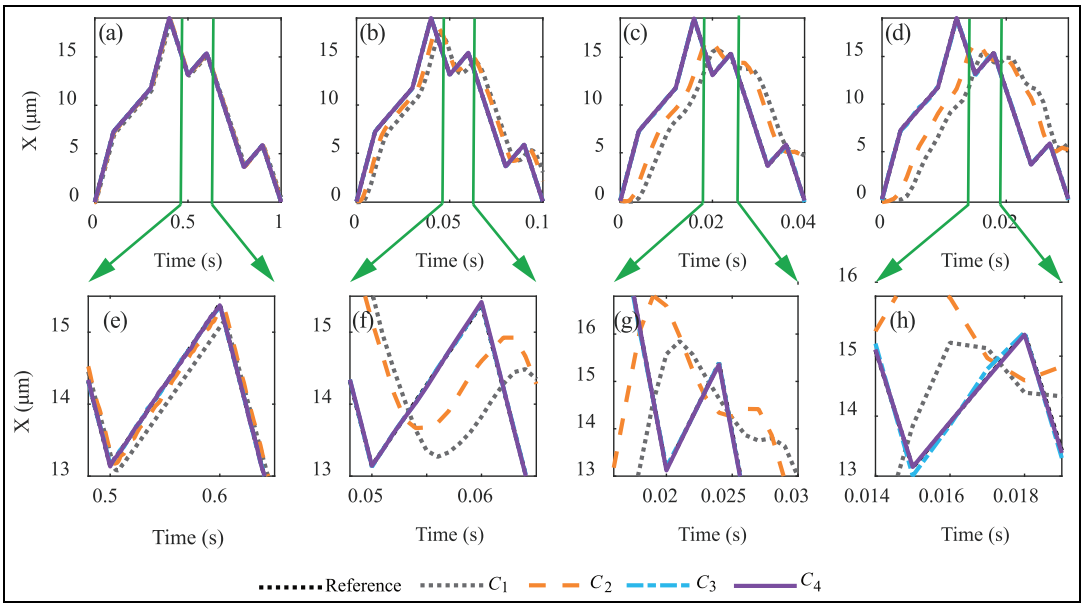

Figure 14. Star trajectory tracking results of *x* axis: (a) 1 s tracking period, (b) 0.1 s tracking period, (c) 0.04 s tracking period, (d) 0.03 s tracking period, and (e)–(h) the zoom-in view.

Table 3. XY star trajectory tracking results.

		x axis				*y* axis			
Statistical errors (nm)		1 s	0.1 s	0.04 s	0.03 s	1 s	0.1 s	0.04 s	0.03 s
C_1	RMS	377.67	2329.12	4416.31	5360.21	397.20	2459.21	5179.94	6596.81
	MAX	785.32	4317.91	8106.52	9251.12	1034.81	5823.83	13298.01	15884.11
C_2	RMS	186.05	1639.41	3236.51	4113.83	186.51	1695.21	3733.24	4745.51
	MAX	310.60	2643.72	5842.41	7438.43	389.67	3656.41	9204.51	11351.11
C_3	RMS	11.36	16.38	72.99	109.81	13.79	26.65	89.71	104.16
	MAX	36.56	37.93	168.40	172.42	40.17	66.56	203.96	169.10
C_4	RMS	10.32	16.24	27.79	24.89	11.32	25.56	38.82	39.03
	MAX	28.97	27.78	70.93	41.05	37.78	54.13	134.08	89.70

RMS: root mean square.

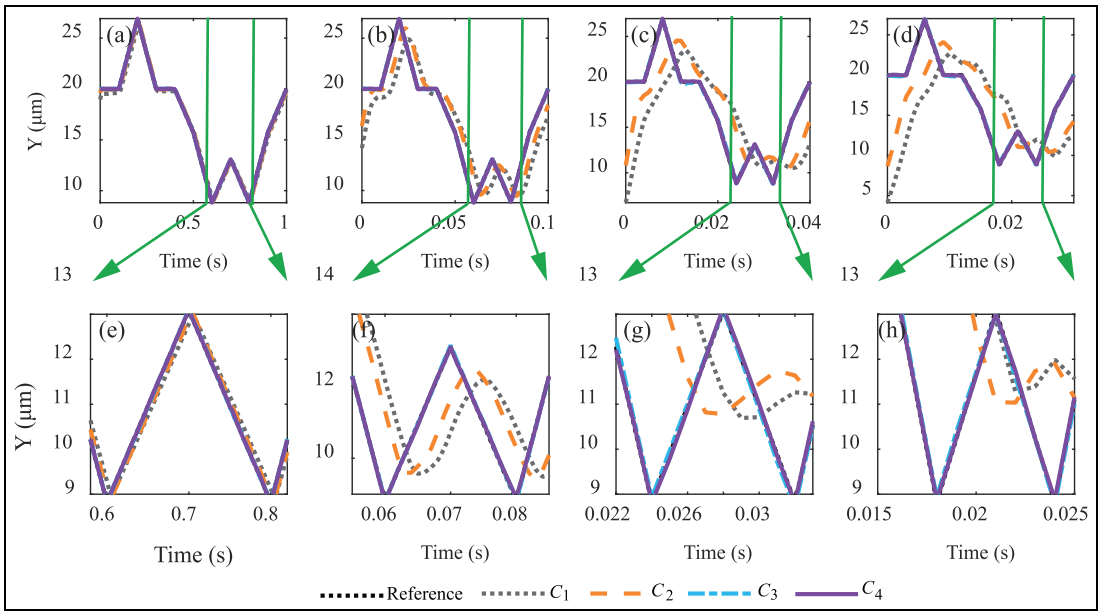

Figure 15. Star trajectory tracking results of *y* axis: (a) 1 s tracking period, (b) 0.1 s tracking period, (c) 0.04 s tracking period, (d) 0.03 s tracking period, and (e)–(h) the zoom-in view.

errors and MAX errors are all below 40 and 89 nm that are equal to 0.21% and 0.46% of the *x* axis scan range 19.02 μm. The similar results can be obtained through the statistical errors of *y* axis.

Conclusion

In this article, the data-based double-feedforward controller was proposed to compensate errors resulted from individual vibrations and cross-coupling errors simultaneously by combing DFDC and MIIC. To alleviate the dependence for accurate modeling and handle the NMP zeros, the controller was designed via the collected data without modeling process. The experimental results on the coupled parallel piezo nanopositioning stage illustrate that cross-coupling errors were suppressed significantly at all frequency region via implementing DFDC. For multi-axis tracking performance, raster scanning and star trajectory were experimented with different tracking periods and it can be concluded that fast and accurate tracking was achieved with the proposed controller through comparative experiments.

Declaration of conflicting interests

The author(s) declared no potential conflicts of interest with respect to the research, authorship, and/or publication of this article.

Funding

The author(s) disclosed receipt of the following financial support for the research, authorship, and/or publication of this article: This work was supported by the Natural Science Foundation of China under Grant 51375349 and Shenzhen Science and Technology Program under Grant JCYJ20170306171514468.

References

1. Devasia S, Eleftheriou E and Moheimani SOR. A survey of control issues in nanopositioning. *IEEE T Contr Syst T* 2007; 15: 802–823.
2. Salapaka SM and Salapaka MV. Scanning probe microscopy. *IEEE Contr Syst* 2008; 28: 65–83.
3. Binnig G, Quate CF and Gerber C. Atomic force microscope. *Phys Rev Lett* 1986; 56: 930.
4. Xu Q and Li Y. Dahl model-based hysteresis compensation and precise positioning control of an XY parallel micromanipulator with piezoelectric actuation. *J Dyn Syst-T ASME* 2010; 132: 041011.
5. Rakotondrabe M, Haddab Y and Lutz P. Development, modeling, and control of a micro-/nanopositioning 2-dof stick–slip device. *IEEE-ASME T Mech* 2009; 14: 733–745.
6. Yong YK, Moheimani SO, Kenton BJ, et al. Invited review article: high-speed flexure-guided nanopositioning: mechanical design and control issues. *Rev Sci Instrum* 2012; 83: 121101.
7. Leang KK and Devasia S. Feedback-linearized inverse feedforward for creep, hysteresis, and vibration compensation in AFM piezoactuators. *IEEE T Contr Syst T* 2007; 15: 927–935.
8. Xu Q. Digital integral terminal sliding mode predictive control of piezoelectric-driven motion system. *IEEE T Ind Electron* 2016; 63: 3976–3984.
9. Fleming AJ and Leang KK. Charge drives for scanning probe microscope positioning stages. *Ultramicroscopy* 2008; 108: 1551–1557.

10. Gu GY, Zhu LM, Su CY, et al. Modeling and control of piezo-actuated nanopositioning stages: a survey. *IEEE T Autom Sci Eng* 2016; 13: 313–332.
11. Gu GY, Li CX, Zhu LM, et al. Modeling and identification of piezoelectric-actuated stages cascading hysteresis nonlinearity with linear dynamics. *IEEE-ASME T Mech* 2016; 21: 1792–1797.
12. Gu GY, Zhu LM and Su CY. Modeling and compensation of asymmetric hysteresis nonlinearity for piezoceramic actuators with a modified Prandtl–Ishlinskii model. *IEEE T Ind Electron* 2014; 61: 1583–1595.
13. Yi J, Chang S and Shen Y. Disturbance-observer-based hysteresis compensation for piezoelectric actuators. *IEEE-ASME T Mech* 2009; 14: 456–464.
14. Li CX, Ding Y, Gu GY, et al. Damping control of piezo-actuated nanopositioning stages with recursive delayed position feedback. *IEEE-ASME T Mech* 2016; 22: 855–864.
15. Clayton GM, Tien S, Leang KK, et al. A review of feedforward control approaches in nanopositioning for high-speed SPM. *J Dyn Syst-T ASME* 2009; 131: 061101.
16. Bhikkaji B, Ratnam M and Moheimani SR. PVPF control of piezoelectric tube scanners. *Sensor Actuat A-Phys* 2007; 135: 700–712.
17. Yao Q, Dong J and Ferreira PM. Design, analysis, fabrication and testing of a parallel-kinematic micropositioning XY stage. *Int J Mach Tool Manu* 2007; 47: 946–961.
18. Li Y and Xu Q. Development and assessment of a novel decoupled XY parallel micropositioning platform. *IEEE-ASME T Mech* 2010; 15: 125–135.
19. Polit S and Dong J. Development of a high-bandwidth XY nanopositioning stage for high-rate micro-/nanomanufacturing. *IEEE-ASME T Mech* 2011; 16: 724–733.
20. Mahmood IA and Moheimani SOR. Making a commercial atomic force microscope more accurate and faster using positive position feedback control. *Rev Sci Instrum* 2009; 80: 063705.
21. Fairbairn MW and Moheimani SO. Resonant control of an atomic force microscope micro-cantilever for active Q control. *Rev Sci Instrum* 2012; 83: 083708.
22. Bhikkaji B and Moheimani SO. Integral resonant control of a piezoelectric tube actuator for fast nanoscale positioning. *IEEE-ASME T Mech* 2008; 13: 530–537.
23. Aphale SS, Ferreira A and Moheimani SR. A robust loop-shaping approach to fast and accurate nanopositioning. *Sensor Actuat A-Phys* 2013; 204: 88–96.
24. Yang MJ, Gu GY and Zhu LM. High-bandwidth tracking control of piezo-actuated nanopositioning stages using closed-loop input shaper. *Mechatronics* 2014; 24: 724–733.
25. Das SK, Pota HR and Petersen IR. Multivariable negative-imaginary controller design for damping and cross coupling reduction of nanopositioners: a reference model matching approach. *IEEE-ASME T Mech* 2015; 20: 3123–3134.
26. Das SK, Pota HR and Petersen IR. Resonant controller design for a piezoelectric tube scanner: a mixed negative-imaginary and small-gain approach. *IEEE T Contr Syst T* 2014; 22: 1899–1906.
27. Lee C and Salapaka SM. Robust broadband nanopositioning: fundamental trade-offs, analysis, and design in a two-degree-of-freedom control framework. *Nanotechnology* 2009; 20: 035501.
28. Guo Y and Mishra S. Constrained optimal iterative learning control with mixed-norm cost functions. *Mechatronics* 2017; 43: 56–65.
29. Bristow DA, Tharayil M and Alleyne A. A survey of iterative learning control. *IEEE Contr Syst Mag* 2006; 26: 96–114.
30. Bristow DA, Dong J, Alleyne AG, et al. High bandwidth control of precision motion instrumentation. *Rev Sci Instrum* 2008; 79: 103704.
31. Yan Y, Wang H and Zou Q. A decoupled inversion-based iterative control approach to multi-axis precision positioning: 3D nanopositioning example. *Automatica* 2012; 48: 167–176.
32. Kim K and Zou Q. A modeling-free inversion-based iterative feedforward control for precision output tracking of linear time-invariant systems. *IEEE-ASME T Mech* 2013; 18: 1767–1777.
33. Bolder J, Kleinendorst S and Oomen T. Data-driven multivariable ILC: enhanced performance by eliminating L and Q filters. *Int J Robust Nonlin*. Epub ahead of print 24 July 2016. DOI: 10.1002/rnc.3611.
34. Heertjes M, Hennekens D and Steinbuch M. MIMO feed-forward design in wafer scanners using a gradient approximation-based algorithm. *Control Eng Pract* 2010; 18: 495–506.
35. Zheng J, Guo G and Wang Y. Feedforward decoupling control design for dual-actuator system in hard disk drives. *IEEE T Magn* 2004; 40: 2080–2082.
36. Liu L, Tan KK, Chen S, et al. Discrete composite control of piezoelectric actuators for high-speed and precision scanning. *IEEE T Ind Inform* 2013; 9: 859–868.
37. Li CX, Gu GY, Yang MJ, et al. High-speed tracking of a nanopositioning stage using modified repetitive control. *IEEE T Autom Sci Eng* 2015; 14: 1467–1477.
38. Hu C, Yao B and Wang Q. Coordinated adaptive robust contouring control of an industrial biaxial precision gantry with cogging force compensations. *IEEE T Ind Electron* 2010; 57: 1746–1754.
39. Chen CS and Chen LY. Robust cross-coupling synchronous control by shaping position commands in multiaxes system. *IEEE T Ind Electron* 2012; 59: 4761–4773.
40. Ljung L. *System identification: theory for the user*. 2th ed. Upper Saddle River, NJ: Prentice Hall, 1999.